Asymptotics of gravitational collapse of scalar waves

R. Gómez and J. Winicour
Department of Physics and Astronomy, University of Pittsburgh, Pittsburgh, Pennsylvania 15260

(Received 28 March 1991; accepted for publication 20 November 1991)

Through a combination of analytic and numerical techniques, the formation of a black hole by a self-gravitating, spherically symmetric, massless scalar field is investigated. The evolution algorithm incorporates a Penrose compactification so that the Bondi mass, the news function, and other radiation zone limits can be obtained numerically. The late time behavior recently established by Christodoulou is confirmed and new asymptotic relations for late time and for large amplitude limits are derived. For example, it is shown, that the Bondi mass M_B and the scalar monopole moment Q satisfy the asymptotic relation $M_B \sim \pi|Q|/\sqrt{2}$ at high amplitudes. It is found that the scalar monopole moment decays exponentially during black hole formation in contrast to the perturbation theory result for a power law decay rate in an Oppenheimer–Snyder background. It is demonstrated that the Newman–Penrose constant for the scalar field is globally well defined and has significant effects.

I. INTRODUCTION

In this paper, we investigate black hole formation by a spherically symmetric, general relativistic, asymptotically flat, zero rest mass Klein–Gordon field. Our most important new results are (i) in the strong field limit, the Bondi mass equals the scalar field monopole moment, up to a universal constant; (ii) during black hole formation the monopole moment decays exponentially with respect to a distant observer, rather than as the power law predicted by perturbation theory; and (iii) the Newman–Penrose constant for the scalar field significantly affects the late stage of gravitational collapse.

The first of these results is purely analytic and derives from a novel application of the method of Laplace to obtain asymptotic formulas for the scaling behavior of the mass, as described in Sec. III. The other two results are partially based upon numerical simulations, whose methodology is described in Sec. IV. Result (ii), discussed in Secs. V and VI, is based upon a nonlinear version of Price's[1] model of a test scalar field on an Oppenheimer–Snyder background. Price showed that an initially smooth test field would evolve across the horizon without developing a singularity and that its monopole moment would be completely radiated away. His work furnished the impetus for the no-hair picture of black holes. Result (iii) establishes the manner in which the Newman–Penrose constant[2] for the scalar field is consistent with the no-hair scenario. Perturbation arguments have questioned the appropriate asymptotic region in which the Newman–Penrose constant is well defined.[3,4] Our results demonstrate that the Newman–Penrose constant is globally well defined at future null infinity J^+, that it is indeed conserved, and that it can lead to nontrivial qualitative effects. This is presented in Sec. VI, along with an overview of the main features of the energetics and asymptotics of black hole formation for a variety of initial waveforms. The numerical algorithm incorporates a Penrose compactification that allows the first illustrations of the conformal singularity forming at future time infinity I^+.

Christodoulou[5–8] has made a penetrating analysis of the existence and uniqueness of solutions describing gravitational collapse of a scalar field, in the spherically symmetric scalar case, and has established a rigorous version of the no-hair theorem. Working in the framework of the characteristic initial value problem on an outgoing null cone, he proved that weak initial data evolves to Minkowski space asymptotically in time but that sufficiently strong data forms a horizon, with nonzero final Bondi mass $M_{\mathscr{H}}$ and zero scalar monopole moment. The geometry is asymptotically Schwarzschild in the approach to I^+ outside the sphere $r = 2M_{\mathscr{H}}$. Figure 1 depicts such a field beginning at initial retarded time u_0 and forming a horizon at u_H. The situation is akin to the Oppenheimer–Snyder collapse except for the radiation to J^+, whose backscatter causes the $r = 2M_{\mathscr{H}}$ curve to intersect the horizon only in an asymptotic limit at I^+.

II. FORMALISM AND BACKGROUND

We begin with a brief description of the Bondi formalism for the model and of Christodoulou's main results. The spherically symmetric solutions of Einstein's equation for a zero rest mass scalar field Φ,

$$G_{\mu\nu} = 8\pi[\nabla_\mu\Phi\,\nabla_\nu\Phi - \tfrac{1}{2}g_{\mu\nu}\,\nabla_\alpha\Phi\,\nabla^\alpha\Phi], \tag{2.1}$$

have a characteristic initial value formulation based upon outgoing null cones emanating from the central geodesic.[9] Let the coordinate u be the proper time along this geo

 0022-2488/92/041445-13$03.00

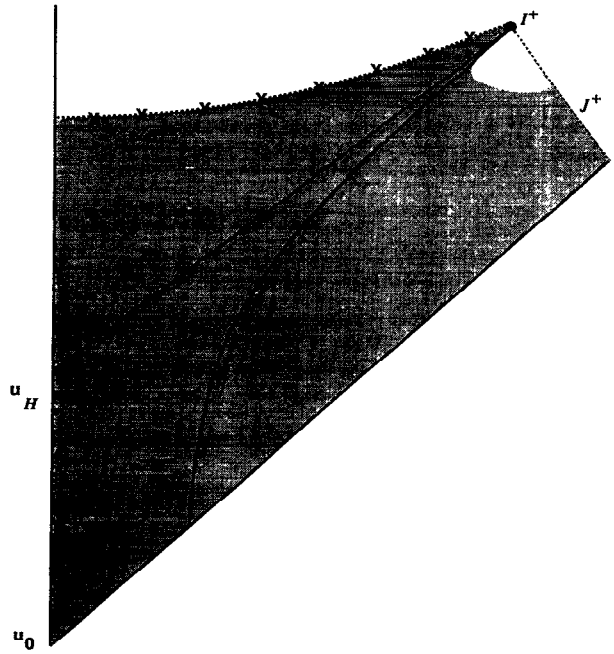

FIG. 1. A collapsing scalar field. An asymptotically Schwarzschild geometry arises in the approach to I^+ in the nonshaded region.

desic, with $u = \text{const}$ on the outgoing null cones. Let r be a surface-area distance on these null cones. Then, in the corresponding Bondi coordinate system, the line element takes the form

$$ds^2 = e^{2\beta}\, du[(V/r)du + 2\, dr] - r^2(d\theta^2 + \sin^2\theta\, d\phi^2), \tag{2.2}$$

where θ and ϕ are the usual polar coordinates. At $r = 0$, we adopt as coordinate conditions

$$V(u,r) = r + O(r^3) \quad \text{and} \quad \beta(u,r) = O(r^2), \tag{2.3}$$

so that the metric reduces to a Minkowski (null polar) form along the central worldline. The resulting metric does not take an asymptotic Minkowski form in the limit $r \to \infty$ of J^+. We set $H(u) = \beta(u,\infty)$. Then Bondi time $\tilde{u}$ for a Minkowski frame at J^+ is related to proper time u along the central geodesic by

$$\frac{d\tilde{u}}{du} = e^{2H}. \tag{2.4}$$

The coordinates $\tilde{u}$, r, θ, and ϕ constitute a standard Bondi frame whose line element is given by (2.2) with the replacements $V \to \tilde{V} = e^{-2H}V$ and $\beta \to \tilde{\beta} = \beta - H$. Bondi time $\tilde{u}$ is more convenient in discussing asymptotic quantities such as the mass and news function. However, central time u is more convenient in dealing with horizons. A horizon forms at a finite central time $u = u_{\mathscr{H}}$ but at an infinite Bondi time $\tilde{u}_{\mathscr{H}} = \infty$, with the central redshift determined by Eq. (2.4).

The field equations are equivalent to the two hypersurface equations:

$$\beta_{,r} = 2\pi r(\Phi_{,r})^2, \tag{2.5}$$

$$V_{,r} = e^{2\beta}, \tag{2.6}$$

and the scalar wave equation $\Box\Phi = 0$, which in Bondi coordinates takes the form

$$2(r\Phi)_{,ur} = r^{-1}(rV\Phi_{,r})_{,r}. \tag{2.7}$$

Initial null data for evolution consists of $\Phi(u_0,r)$ at initial time u_0. We use the gauge freedom $\Phi \to \Phi + \text{const}$ to set $\Phi(u_0,\infty) = 0$. Furthermore, we only consider nonsingular, asymptotically flat data satisfying the smoothness conditions

$$g(u_0,0) = 0, \quad g(u_0,\infty) = Q(u_0) \quad \text{and} \quad \partial_r^n g(u_0,\infty) = 0, \quad \text{for } n \neq 0, \tag{2.8}$$

where $g = r\Phi$ and $Q(u)$ is the scalar monopole moment. By radial integration of the hypersurface equations [(2.5) and (2.6)] using the boundary conditions (2.3), this data uniquely determines, in turn, $\beta(u_0,r)$ and $V(u_0,r)$. Formal evolution then proceeds by determining $\partial_u\Phi(u_0,r)$ from the radial integral of the wave equation (2.7), which gives, after integration by parts,

$$2r\Phi_{,u} = V\Phi_{,r} + \int_0^r \left(\frac{V}{r}\right)\Phi_{,r}\, dr. \tag{2.9}$$

This formally preserves the smoothness conditions, i.e., $\partial_u g$ satisfies the analog of (2.8).

Asymptotic quantities of special physical interest are the Bondi mass

$$M(u) = \tfrac{1}{2}e^{-2H}r^2(V/r)_{,r}|_{r=\infty} \tag{2.10}$$

and the scalar news function

$$N(u) = e^{-2H}Q_{,u}(u). \tag{2.11}$$

Here Q is the scalar monopole moment and the factors of e^{-2H} arise from the relation of central time to Bondi time. The Bondi mass loss equation is

$$e^{-2H}M_{,u} = -4\pi N^2. \tag{2.12}$$

The Bondi mass may be reexpressed as a null cone integral in the three different forms:

$$M=\frac{1}{2}\int_0^\infty [1-e^{2(\beta-H)}]dr$$

$$=2\pi\int_0^\infty e^{2(\beta-H)}r^2(\Phi_{,r})^2\,dr$$

$$=2\pi\int_0^\infty rVe^{-2\beta}(\Phi_{,r})^2\,dr. \tag{2.13}$$

The news function can be also be reexpressed as a null cone integral,

$$N=\frac{1}{2}e^{-2H}\int_0^\infty \frac{V}{r}\Phi_{,r}\,dr, \tag{2.14}$$

as follows immediately from (2.9). In the flat space case, for which $V=r$, this integrates to give $N=-\frac{1}{2}\Phi(u,0)$, which equates the signal at null infinity to the signal arriving at the origin. In the curved space case, the *News Function Mean Value Theorem*[10] gives a related result:

$$N=-\tfrac{1}{2}\Phi(u,\xi), \tag{2.15}$$

for some value $0\leqslant\xi\leqslant\infty$. This provides insight into the limitations of backscattering in constructively rechanneling incoming waves to produce high-amplitude outgoing radiation. No matter how contrived the incoming fields might be at a given retarded time, the resulting news function is restricted by the maximum magnitude of Φ.

Assuming that the scalar field has an asymptotic expansion,

$$\Phi=Q(u)/r+Q_2(u)/r^2+\cdots, \tag{2.16}$$

then an expansion of the scalar wave equation implies that $Q_{2,u}=0$. Q_2 is the Newman–Penrose constant for the scalar field.[2] Also of interest is the positive quantity

$$P=4\pi\int_0^\infty r(g_{,r})^2\,dr. \tag{2.17}$$

$P^{1/2}$, like the square root of the Bondi mass, provides a norm on the vector space of asymptotically flat initial data. Using the field equations and boundary condition, integration by parts leads to

$$P_{,\tilde{u}}=e^{-2H}P_{,u}=\frac{1}{2}\int_0^\infty [1-e^{2(\beta-H)}$$

$$+4(\beta-H)e^{2(\beta-H)}]dr. \tag{2.18}$$

Besides the asymptotics of the neighborhood of J^+, there is the important but more difficult issue of asymptotic behavior in the neighborhood of I^+. When the final Bondi mass vanishes, this behavior is analogous to that for linear waves in a Minkowski background. When a horizon forms, Christodoulou's[8] powerful results supply some of the key features. Let the horizon form at $u=u_{\mathscr{H}}$ with Bondi mass $M_{\mathscr{H}}$. Then the geometry has the asymptotic behavior

$$e^{2(\beta-H)}\to\begin{cases}0, & \text{for } r<2M_{\mathscr{H}},\\ 1, & \text{for } r>2M_{\mathscr{H}},\end{cases} \tag{2.19}$$

in the limit $u\to u_{\mathscr{H}}$. Referring to (2.13) and (2.18), this implies that P becomes singular at the rate

$$P\sim M_{\mathscr{H}}\tilde{u}, \tag{2.20}$$

with respect to Bondi time, during the formation of a horizon.

III. SCALING

Two types of one-parameter scale freedom play a natural role in this system. Metric rescaling, defined by $g_{\mu\nu}\to a^2g_{\mu\nu}$, $\Phi\to\Phi$ leaves the Einstein equation (2.1) invariant, leads to no essentially new physics, and merely changes the length and time scales. Formation of a horizon is invariant under metric rescaling. The mass of the horizon is not invariant and can be made arbitrarily small or large by rescaling. By means of the coordinate transformation $u\to u/a$, $r\to r/a$, metric rescaling may be reexpressed as $\beta(u,r)\to\beta(u/a,r/a)$, $V(u,r)\to V(u/a,r/a)$, and $\Phi(u,r)\to\Phi(u/a,r/a)$.

The other freedom, amplitude scaling, pertains to rescaling the null data. For given initial data, the one-parameter family of rescaled data $\Phi(u_0,r;\lambda)=\lambda\Phi(u_0,r)$ preserves asymptotic flatness but, unlike metric scaling, does not commute with evolution, $\Phi(u_1,r;\lambda)\neq\lambda\Phi(u_1,r)$, except in the small λ linearized limit. In that limit, energy scales quadratically $M(u;\lambda)\sim\lambda^2M(u)$ and the news function scales linearly, $N(u;\lambda)\sim\lambda N(u)$.

In the opposite large λ extreme, interesting saturation effects occur. From the hypersurface equations (2.5) and (2.6), we find

$$\beta(u_0,r;\lambda)=\lambda^2\beta(u_0,r) \tag{3.1}$$

and

$$V(u_0,r;\lambda)=\int_0^r e^{2\lambda^2\beta(u_0,r)}\,dr. \tag{3.2}$$

The second mass expression (2.13) then gives

$$M(\lambda)=2\pi\lambda^2\int_0^\infty e^{2\lambda^2(\beta-H)}r^2(\Phi_{,r})^2\,dr, \tag{3.3}$$

where we suppress the implicit dependencies on u_0 and r but indicate all λ dependence.

This mass integral has the appropriate structure for extracting its large λ dependence by means of the method of Laplace.[11] This method gives the asymptotic large τ behavior of the integral,

$$I(\tau,a,b)=\int_a^b f(x)e^{\tau h(x)}\,dx, \tag{3.4}$$

where $h(b)>h(x)$ for $a\leqslant x<b$, by (i) introducing the truncated integral $I(\tau,b-\epsilon,b)$, (ii) replacing $f(x)$ and $h(x)$ in $I(\tau,b-\epsilon,b)$ by the leading terms in their Taylor expansions about $x=b$, and (iii) evaluating the resulting integral in the limit $\epsilon\to\infty$.

The application of this method to $M(\lambda)$ depends upon the large r behavior of Φ. First, suppose Φ contains a monopole moment so that $\Phi\sim Q/r$. Then β attains its maximum H asymptotically at infinity, with

$$\beta=H-(\pi Q^2/r^2)+O(1/r^3), \tag{3.5}$$

according to the expansion of (2.5). By introducing the new integration variable $x=r/(1+r)$, the integration limits are compactified between $x=0$ and $x=1$. The method of Laplace can then be applied in a straightforward manner to (3.3), which leads to

$$M(\lambda)\sim 2\pi\lambda^2Q^2\int_{-\infty}^{1} e^{-2\pi\lambda^2Q^2(x-1)^2}\,dx. \tag{3.6}$$

Integration then gives

$$M(u_0;\lambda)\sim(\pi/\sqrt{2})\,|Q(u_0;\lambda)|. \tag{3.7}$$

In this regime, the mass is essentially the magnitude of the monopole moment! The approximation

$$M\approx(\pi/\sqrt{2})\,|Q| \tag{3.8}$$

provides a necessary condition that can be used to test whether the field is in the high-amplitude regime, at any retarded time such that $Q\neq 0$. The method of Laplace can be used to extend the asymptotic relation (3.7) to higher order. In terms of the conserved quantity Q_2 in (2.16),

$$M\sim\frac{\pi}{\sqrt{2}}\,|Q|+\frac{2Q_2}{3Q}+O\left(\frac{1}{\lambda}\right). \tag{3.9}$$

Next, consider the case that the initial data Φ has compact support, with R the smallest value of r outside of which $\Phi=0$. Then β attains its maximum H at $r=R$, so that the method of Laplace can then be applied directly in terms of the integration variable r, with integration limits between 0 and R. This gives

$$M(u_0;\lambda)\sim R/2. \tag{3.10}$$

In the intermediate case with $Q=0$ and $\Phi=O(1/r^p)$, $M(u_0;\lambda)$ has $O(\lambda^{1/p})$ asymptotic dependence ($p\geqslant 1$).

Compare these results to the weak field limit,

$$M(\lambda)\sim 2\pi\lambda^2\int_0^\infty r^2(\Phi_{,r})^2\,dr, \tag{3.11}$$

in which M depends quadratically on λ. In the strong field case, (3.7) and (3.10) indicate how a redshift-type effect weakens this dependence. In the noncompact case, M depends at most linearly on λ with the dominant contribution coming from the far-field monopole moment, which is least affected by redshifting. In the compact case, redshifting completely saturates the λ dependence and the null data approaches that for a horizon at $R=2M$. The study of a specific analytic model[10] with compact null data also shows that the news function is completely redshifted away, $N(\lambda)\to 0$ as $\lambda\to\infty$ holding R constant.

If time evolution commuted with amplitude scaling then (3.7) would imply the asymptotic relation

$$M_{,\tilde{u}}(u_0;\lambda)\sim-(\pi/\sqrt{2})\,|Q_{,\tilde{u}}(u_0;\lambda)|. \tag{3.12}$$

In turn, the relations (2.11) and (2.12) between mass loss, news, and monopole change, would then imply that

$$M_{,\tilde{u}}(u_0;\lambda)\sim-\pi/8 \quad\text{and}\quad N(u_0;\lambda)\sim\sqrt{2}/8, \tag{3.13}$$

in the high-amplitude limit. Although these relations are hypothetical, they provide benchmarks for comparison with the actual evolution of high-amplitude data.

The quantity P defined in (2.18) scales quadratically with respect to λ. From the λ-dependent versions of (2.13) and (2.18), its derivative with respect to Bondi time can be expressed in the form

$$P_{,\tilde{u}}=M-\lambda\,\partial_\lambda M. \tag{3.14}$$

In the linear regime, the Bondi mass scales quadratically so that $\lambda\,\partial_\lambda M\sim 2M$ and (3.14) reduces to $P_{,\tilde{u}}\sim -M$. Thus P must monotonically decrease in the weak field regime. Since P is a norm for Φ, this explains how flat space-time arises as a basin of attraction for the weak field case. On the other hand, our prior result (3.9) for the high-amplitude scaling of M implies that

$$P_{,\tilde{u}}\sim 2Q_2/3Q+O(1/\lambda), \tag{3.15}$$

in the generic case $Q\neq 0$. This can be either positive or negative (or zero) depending upon the relative signs of Q and Q_2. Thus the conserved quantity Q_2 has an important qualitative effect on the evolution of a high-amplitude field.

IV. NUMERICAL SOLUTION

Numerical algorithms for a spherically symmetric self-gravitating massless scalar field have been previously developed by Goldwirth and Piran,[12] in a study of cosmic censorship, and by Choptuik,[13] in a study of the sensitivity of black hole formation to initial data. Here we use a curved space version of a nonspherical algorithm developed for nonlinear wave equations in flat space-time.[14,15] In the spherically symmetric case, it has similarities to the Goldwirth–Piran algorithm. A major difference is the use of a numerical grid that compactifies J^+ so that it is well suited for investigating asymptotic properties. Also, the underlying numerical implementation and convergence analysis differ appreciably from the Goldwirth–Piran code and the Courant limit automatically halts the evolution at I^+.

The numerical grid is based upon the outgoing null cones and the compactified radial coordinate $x = r/(1 + r)$. Thus points at J^+ are included in the grid at $x = 1$. In terms of x and $g = r\Phi$, the asymptotic expansion (2.16) takes the form

$$g = Q + Q_2(1 - x) + \cdots, \tag{4.1}$$

so that the the Newman–Penrose constant Q_2 equals the negative of the slope of g at J^+. We use constant grid displacements Δu and Δx. On a given null cone, the hypersurface equations (2.5) and (2.6) are handled by numerical integration. Numerical evolution, from null cone to null cone, is based upon an integral relation equivalent to the scalar wave equation (2.7).

In order to describe this scheme quantitatively, first consider the flat space wave equation, obtained by setting $V = r$ and $\beta = 0$. Let Σ denote the null parallelogram formed by incoming and outgoing radial null rays in the (u,r) plane that intersect at vertices P, Q, R, and S, as depicted in Fig. 2. In the case of spherical symmetry, $g = r\Phi$ obeys the two-dimensional wave equation intrinsic to this plane, whose surface integral over Σ implies the null parallelogram relation $g_Q = g_P + g_S - g_R$. Now consider the curved space case, with Σ formed out of the curved space null rays. The (u,r) submanifold has the intrinsic metric

$$h_{\mu\nu}\, dx^\mu\, dx^\nu = e^{2\beta}\, du[(V/r)du + 2\, dr], \tag{4.2}$$

and the wave equation for g reduces to

$$\Box^{(2)}g + (V/r)_{,r}(e^{-2\beta}g/r) = 0, \tag{4.3}$$

where $\Box^{(2)}$ is the D'Alembertian associated with $h_{\mu\nu}$. In two dimensions, the geometry is conformally flat, the wave operator has conformal weight -2 and the surface area element has conformal weight 2, so that the surface integral of $\Box^{(2)}g$ over Σ gives exactly the flat space result.

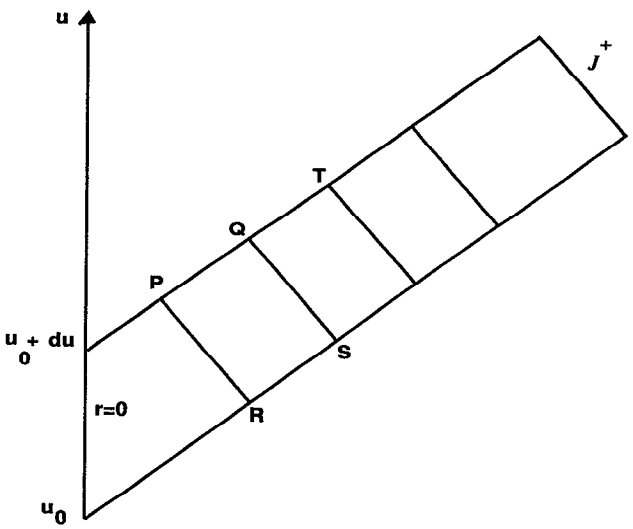

FIG. 2. Scheme for the marching algorithm.

Upon integration of (4.3), curvature introduces an area integral correction to the flat space null parallelogram relation, giving

$$g_Q = g_P + g_S - g_R - \frac{1}{2}\int_\Sigma du\, dr \left(\frac{V}{r}\right)_{,r} \frac{g}{r}. \tag{4.4}$$

This identity gives rise to an explicit marching algorithm for evolution. Let the null parallelogram span null cones at adjacent grid values u_0 and $u_0 + \Delta u$, as shown in Fig. 2, for some θ and ϕ. Imagine for now that the points P, Q, R, and S lie on the grid, so that $x_Q - x_P = x_S - x_R = \Delta x$. If g has been determined on the entire u_0 cone and on the $u_0 + \Delta u$ cone radially outward from the origin to the point P, then (4.4) determines g at the next radial grid point Q in terms of an integral over Σ. The integrand can be approximated to second order, i.e., to $O(\Delta x\, \Delta u)$, by evaluating it at the center of Σ. To the same accuracy, the value of g at the center equals its average between the points P and S, at which g has already been determined. Similarly, the value of $(V/r)_{,r}$ at the center can be approximated to second order in terms of values of V at points where it has already been determined.

After carrying out this procedure to evaluate g at the point Q, the procedure can be repeated to determine g at the next radially outward grid point, the point T in Fig. 2. After completing this radial march to null infinity, the field g is then evaluated on the next null cone at $u_0 + 2\,\Delta u$, beginning at the vertex where smoothness gives the startup condition that $g = 0$.

In practice, the points P, Q, R, and S cannot be chosen to lie exactly on the grid because the velocity of light in terms of the compactified coordinate x is not constant even in flat space. As a consequence, the fields g, β, and V at the vertices of the null parallelogram, i.e., P, Q, R, and

S, are approximated to second order by interpolating between grid points. However, cancellations arise between these four interpolations so that Eq. (4.4) is satisfied to fourth-order accuracy. The net result is that the numerical version of (4.4) steps g radially outward one zone with an error of fourth order in grid size. In addition, the smoothness conditions (2.3) are incorporated into the startup for the numerical integrations for V and β to ensure no loss of accuracy at the boundary $r=0$. The resulting global error in g, after evolving a finite retarded time, is then $O(\Delta u\,\Delta x)$ after compounding errors from $1/(\Delta u\,\Delta x)$ number of zones. Second-order global accuracy is indeed confirmed by convergence tests of the code.

Because of the explicit nature of this algorithm, its stability depends upon an analog of the Courant condition that the physical domain of dependence be contained in the numerical domain of dependence. In the present spherically symmetric case, this condition requires that the ratio of the time step size to radial step size be limited by $(V/r)\Delta u \leqslant 2\,\Delta r$, where $\Delta r = \Delta[x/(1-x)]$. This condition is built into the code using the value $V/r = e^{2H}$, corresponding to the maximum of V/r at J^+. The strongest restriction on the time step arises just before the formation of a horizon. In this limit, $V/r \to \infty$ so that the conformal singularity at I^+ freezes the numerical evolution. In order to evolve across the horizon, exterior radial points must be dropped from the domain of the grid.

V. STATIC–STATIC DATA

The numerical evolution of characteristic initial data induced by pasting an initially static monopole to a flat interior provides a nonlinear version of the test-field problem treated by Price.[1] This example demonstrates several important physical properties.

The simplest static, spherically symmetric, self-gravitating zero rest mass scalar field is $\Phi = \text{const}$, which is pure gauge and not by itself physically interesting. A static solution, which is the analog of the solution $\Phi = 1/r$ in a Minkowski background,[16] can be obtained by setting $\Phi_{,u} = 0$ in the wave equation (2.7). This gives

$$rV\Phi_{,r} = \text{const}, \tag{5.1}$$

whose solution is

$$\Phi(V) = \frac{1}{2\cosh\alpha}\ln\left[\frac{V + R(e^{2\alpha}-1)}{V + R(e^{-2\alpha}-1)}\right], \tag{5.2}$$

with $V(r)$ given implicitly by

$$r^2 = e^{-4\alpha\tanh\alpha}[V + R(e^{-2\alpha}-1)]^{1-\tanh\alpha} \times [V + R(e^{2\alpha}-1)]^{1+\tanh\alpha}. \tag{5.3}$$

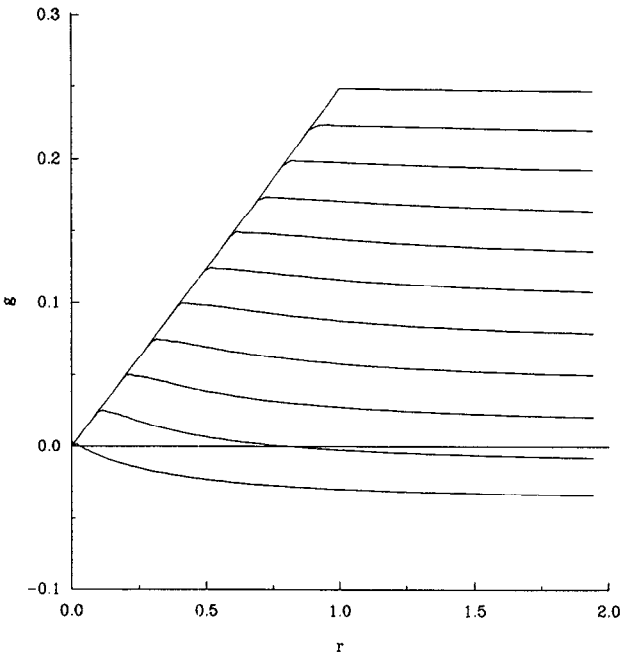

FIG. 3. Evolution of static–static data to flat space.

Here R fixes the length scale and α determines the scalar monopole. The space-time has a naked singularity if it is extended to $r=0$.

Static–static initial null data at $u = u_0$ can be constructed by setting $\Phi(u_0,r) = \Phi_0 = \text{const}$ for $r \leqslant R$ and $\Phi(u_0,r) = \Phi(V)$, as given in Eq. (5.2), for $r \geqslant R$, choosing Φ_0 to make the data continuous. However, the evolution of this data does not remain static. There are two distinct regions, separated by the radially incoming characteristic curve $\mathcal{N}$ through $r=R$ at $u = u_0$. This characteristic is a shock front across which the curvature has a jump discontinuity. To the past of $\mathcal{N}$, the field remains constant and the metric flat, until time $u = 2R$ when $\mathcal{N}$ intersects the origin. To the future of $\mathcal{N}$, backscattering distorts the initial profile of Φ. For fixed R, there are two distinct types of evolution depending upon the value of Φ_0. (Changing Φ_0 should not be confused with the amplitude scaling discussed in Sec. III.)

A. Decay to flat space

For sufficiently small Φ_0 the system evolves asymptotically to Minkowski space-time. Figures 3 and 4 display the numerical evolution for $\Phi_0 = 0.25$ and $R = 1$. In order to give physical perspective to these results consider first the flat space case, in which $g(u,r)$ would propagate toward the origin as a dispersionless one-dimensional radial wave. The boundary condition $g(u,0) = 0$ corresponds to perfect reflection off the origin, which results in an outgoing wave that propagates instantaneously to J^+ in terms of retarded time u. For static–static data in

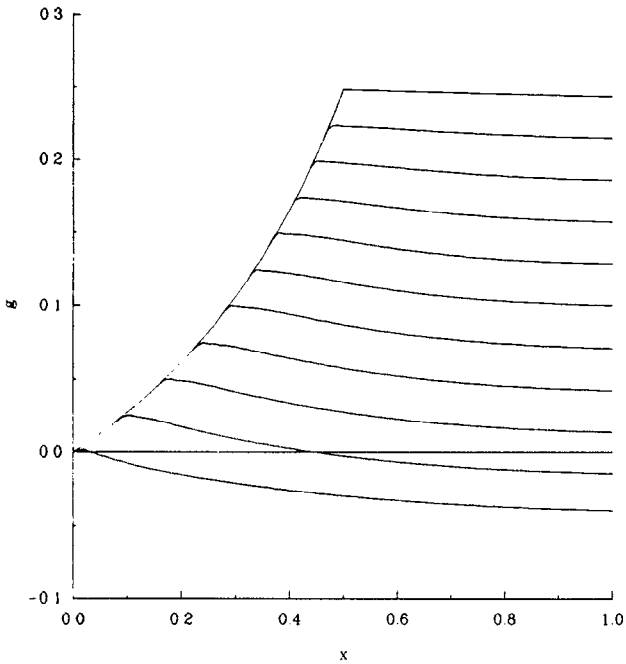

FIG. 4. Evolution to flat space described in the x coordinate.

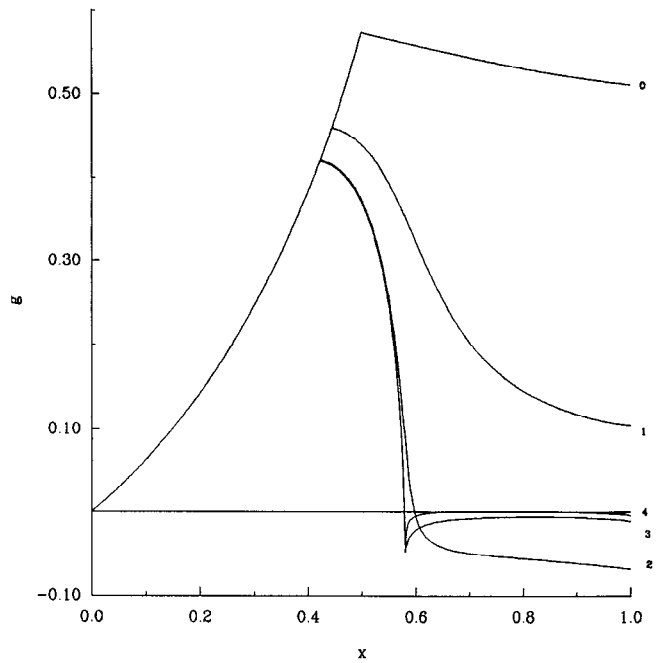

FIG. 5. Evolution of static–static data to a black hole.

the flat space case, g would consist of a piece linear in r, for $r<R$, and a constant piece for $r>R$. Thus, interpreted as a one-dimensional radial wave, all the wave energy would be concentrated in the $r<R$ region and would be propagated to infinity in the time $u_{\mathscr{I}} - u_0 = 2R$ that it takes the incoming characteristic $\mathscr{N}$ to hit the origin. Prior to that time, the system would radiate energy at a constant rate.

Some vestige of this flat space picture, but modified by the dispersive effects of self-gravity, is evident in Fig. 3, which graphs $g(u,r)$ vs r at several retarded times. It distinctly illustrates the breakdown of Huyghen's principle due to curvature. The numerical code handles the propagation of the shock front without any substantial difficulty. It introduces some slight high-frequency numerical noise just outside the shock front, but too small to be perceptible in the figure.

Figure 4 displays the global behavior in terms of a graph of $g(u,x)$ vs $x = r/(1+r)$, between times u_0 and $u_{\mathscr{I}}$. Comparison with Fig. 3 gives an idea of the distortion of the wave profile introduced by the x coordinate. In accord with Eq. (4.1), the value of g at J^+ $(x=1)$ equals the monopole moment Q and the negative of the slope of g at J^+ equals the Newman–Penrose constant Q_2. It is evident from Fig. 4 that the numerical evolution conserves Q_2. Except for these interesting theoretical aspects, the evolution is otherwise boring.

B. Horizon formation

For $R=1$, our numerical results show that the system forms a horizon when $\Phi_0 > 0.286$. Figure 5 illustrates the evolution of $g(u,x)$ for $\Phi_0 = 0.574$. The early stage of the evolution appears innocuous but then the outer region of the profile flattens. This marks the beginning of the process of "shedding hair" as a black hole starts to form. As this process intensifies in the late stage, a cusp begins to form near $r = 2M_{\mathscr{H}}$, where $M_{\mathscr{H}} = M(u_{\mathscr{H}})$ with $u_{\mathscr{H}}$ the time at which the horizon forms. The cusp corresponds to the conformal singularity developing at I^+. Figure 6 graphs $e^{2(\beta - H)}$ at late times just prior to horizon formation. The step function limit (2.19), predicted by Christodoulou, is clear. The graph also shows the accurate agreement between the locations of the step function and the $r = 2M_{\mathscr{H}}$ surface, where the final Bondi mass of the black hole $M_{\mathscr{H}}$ is numerically computed. Here the three formulas for the Bondi mass (2.13) give almost identical numerical values. Outside the $r = 2M_{\mathscr{H}}$ surface, $\Phi \to 0$ and the geometry approaches the Schwarzschild geometry in the limit of I^+, again in agreement with Christodoulou's results portrayed in Fig. 1.

Figure 7 graphs the dependence of the monopole moment on central time. After a long swan dive to a negative value, it rises abruptly to zero just before the horizon forms. The numerical evolution is stopped just short of the horizon due to the inability of the grid to resolve the cusp. The redshift factor at this time is $d\tilde{u}/du \approx 10^7$. According to perturbation calculations[1] for a test scalar

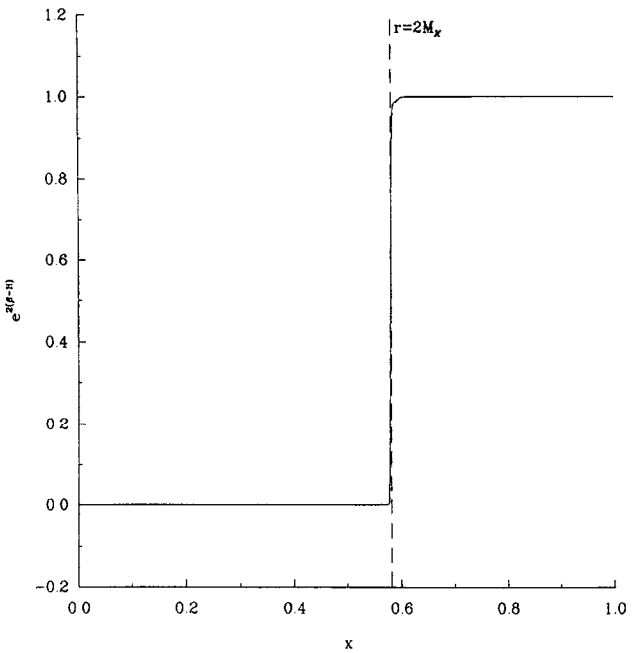

FIG. 6. Formation of a step function.

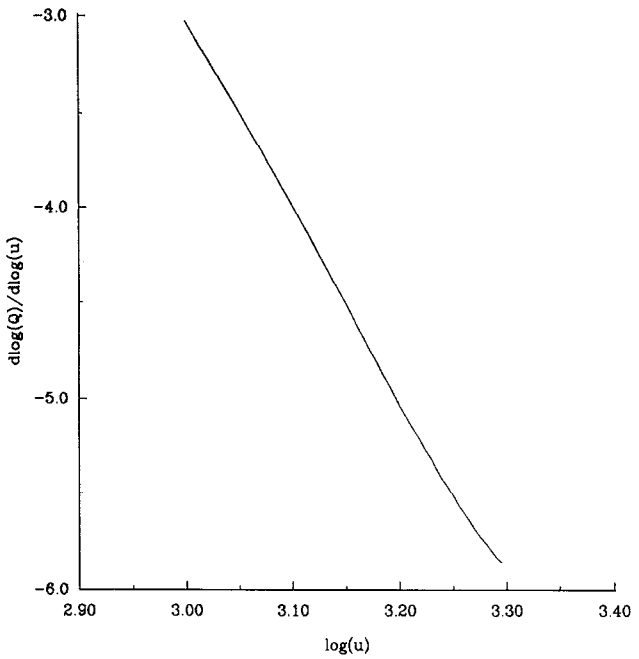

FIG. 8. The logarithmic derivative.

field, the monopole moment should decay as $1/\tilde{u}^2$ with respect to Bondi time. This would correspond to a value $s = -2$ of the logarithmic derivative $s = d \log|Q(\tilde{u})|/d \log \tilde{u}$ plotted in Fig. 8 for the final phase of evolution. The plot shows no agreement with the perturbation theory prediction. This is surprising since in this final phase the metric is very close to a Schwarzschild metric in the region exterior to $r = 2M_{\mathscr{H}}$. The decay of the monopole with respect to central time is very closely approximated by $(u_{\mathscr{H}} - u)^{1/2}$, as can be seen in Fig. 9, which plots Q^2 for the same time interval used in Fig. 8. Although we

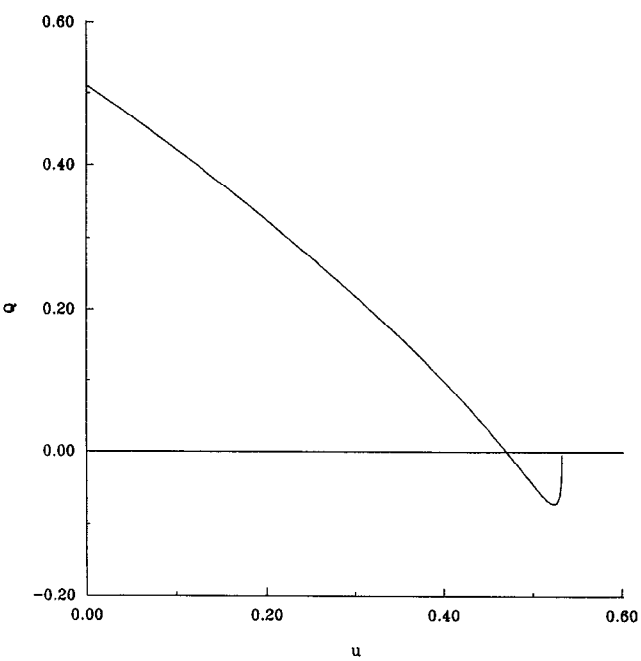

FIG. 7. Decay of the monopole for static–static data.

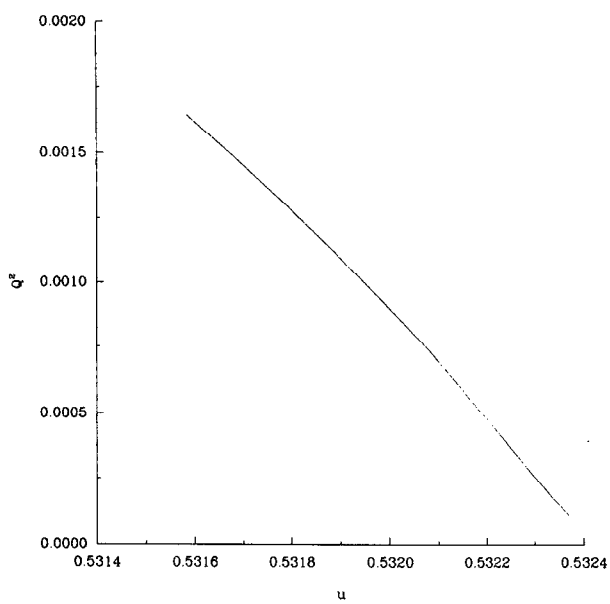

FIG. 9. The square of the monopole for static–static data.

have no rigorous derivation of this behavior, it corresponds to the predictions of the following toy model.

C. A toy model

Some aspects of the bifurcation phenomenon, which separates evolution to flat space from evolution to a horizon, can be modeled in the following simple way. The values of the monopole moment Q and the radius of the shock front R determine unique static–static initial data. In terms of the variable α,

$$Q=2R\sinh\alpha e^{-2\alpha\tanh\alpha}. \tag{5.4}$$

At the initial time u_0, it is easy to integrate the evolution equation (2.7) to find $Q_{,u}$, since the time dependence is purely due to the shock front. This gives

$$Q_{,u}=-\sinh\alpha. \tag{5.5}$$

A toy model with two degrees of freedom Q and R can be extracted by requiring Eqs. (5.4) and (5.5) to hold for all times, supplemented by the condition $R_{,u}=-\frac{1}{2}$, which expresses the constant velocity of the shock front with respect to the flat interior. [Physically, this last equation is sensible only up to the time $u_{\mathscr{I}^-}$ for which $R(u_{\mathscr{I}^-})=0$]. Matching the u derivative of (5.4) to (5.5), we obtain

$$e^{2\alpha\tanh\alpha}-1=2R\alpha_{,u}[2\tanh\alpha-\coth\alpha+2\alpha/\cosh^2\alpha]. \tag{5.6}$$

Since the left-hand side of (5.6) is positive, α either monotonically increases or decreases depending upon whether the bracketed expression on the right-hand side is positive or negative, respectively. The bracket is a monotonically increasing function of α, which is negative for α below the critical value $\alpha_c\approx 0.586$ and positive above that value. Correspondingly, for $\alpha_0=\alpha(u_0)<\alpha_c$, α decays to zero; and for $\alpha_0>\alpha_c$, α grows to infinity. In either case, according to (5.4), the monopole moment decays to zero. This models the decay of the monopole moment under evolution to either flat space or a horizon.

For small α, corresponding to the weak field case, (5.6) has the limiting form

$$\alpha^3=-R\alpha_{,u}, \tag{5.7}$$

whose solution is

$$\alpha=\alpha_0[1-4\alpha_0^2\log(R/R_0)]^{-1/2}, \tag{5.8}$$

where $R_0=R(u_0)$. Thus α and Q decay to zero at precisely the time $u_{\mathscr{I}^-}$ when $R=0$, in agreement with the flat space limit.

For large α, corresponding to the strong field case, (5.6) has the limiting form

$$e^{-2\alpha}\alpha_{,u}=1/(2R), \tag{5.9}$$

whose solution is

$$e^{-2\alpha}=e^{-2\alpha_0}+2\log(R/R_0). \tag{5.10}$$

Since $\log(R/R_0)\to-\infty$ as $u\to u_{\mathscr{N}}$, there exists some time $u_{\mathscr{H}}$, intermediate between u_0 and $u_{\mathscr{N}}$ such that $\alpha(u)\to\infty$ as $u\to u_{\mathscr{H}}$. In this limit, $Q(u_{\mathscr{H}})=0$. It is possible to extract the asymptotic decay rate of the monopole moment by Taylor expanding the time dependence of (5.10) about $u_{\mathscr{H}}$ and using the large α version of Eq. (5.4), which relates Q to α. This gives

$$Q(u)\sim\sqrt{R_{\mathscr{H}}(u_{\mathscr{H}}-u)}, \tag{5.11}$$

where $R_{\mathscr{H}}=R(u_{\mathscr{H}})$. This is in good agreement with the numerical results shown in Fig. 9.

For small values of $u-u_0$, Eq. (5.6) has the same canonical form as the equation

$$(\alpha-\alpha_c)\alpha_{,u}=\tfrac{1}{2}, \tag{5.12}$$

with solution

$$(\alpha-\alpha_c)=\pm\sqrt{(\alpha_0-\alpha_c)^2+u-u_0}. \tag{5.13}$$

For initial data $\alpha_0<\alpha_c$, the negative root is the correct choice; and for $\alpha_0>\alpha_c$, the positive root. But there is no unique solution for $\alpha_0=\alpha_c$ so that the toy model gives no insight into the critical case.

VI. WAVEFORMS: ENERGETICS AND COLLAPSE

We now present a perspective of the energetics, asymptotics, and scaling properties of a general waveform undergoing collapse to a black hole. We discuss three cases, each adding an additional degree of complexity to the initial wave profile.

A. Example A

First consider the one-parameter set of initial data,

$$\Phi(u_0,r)=\lambda/(1+r). \tag{6.1}$$

The energy is initially concentrated in a spherical shell centered about the radius $r=1$. We are particularly interested in how the features of the collapse depend upon the amplitude scale λ. From numerical experimentation, we find that the critical value for horizon formation is $\lambda_c\approx 1.317$.

Figure 10 gives a log–log graph of the computed values of the initial Bondi mass versus λ. For small λ, the graph is a straight line of slope 2, corresponding to the quadratic λ dependence of the mass in the weak field case. For large λ, the graph is a straight line of slope 1, corresponding to the linear λ dependence in the high-

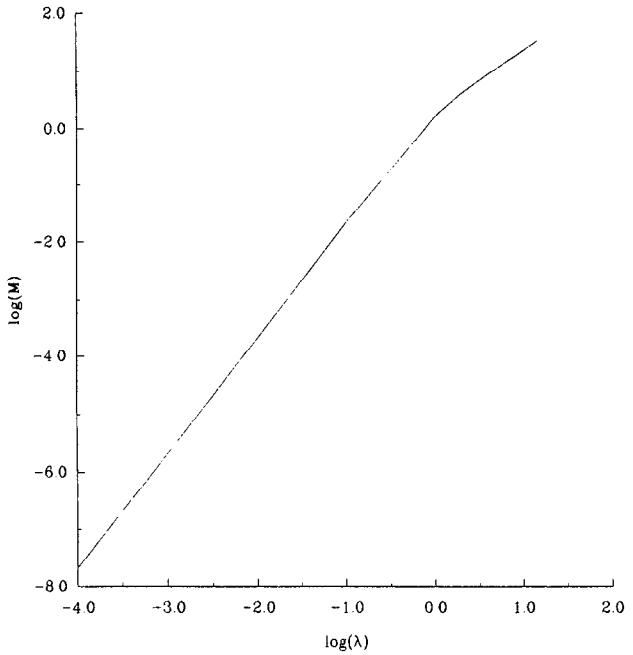

FIG. 10. Scaling of the Bondi mass for example A.

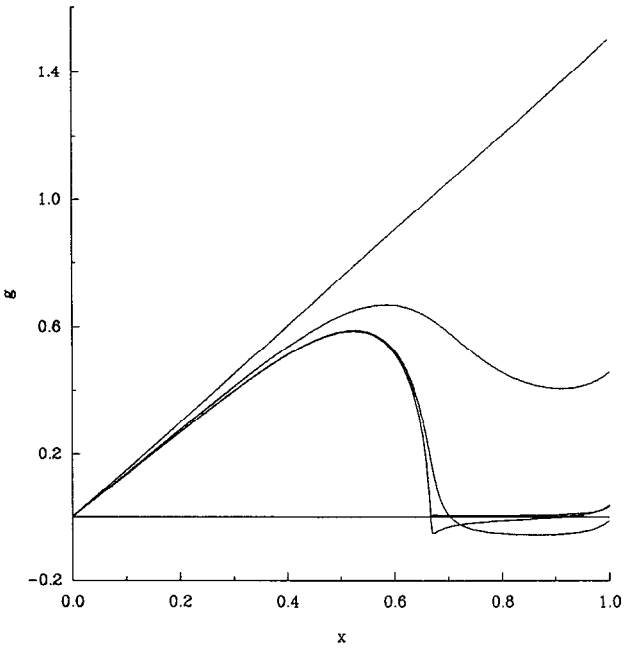

FIG. 12. Evolution of g for example A.

amplitude regime. The critical value λ_c lies in the transition region between quadratic and linear dependence. The graph extends to the value $\lambda = 15$, past which terms in the code of magnitude $e^{-2\lambda}$ lead to excessive numerical underflow. At this value, the computational results agree with the asymptotic relation $M \sim (\pi/\sqrt{2})\,|Q|$, predicted by Eq. (3.7), to 1 part in 10 000. An important point to be appreciated here is that the high-amplitude limit is not out of the reach of numerical treatment.

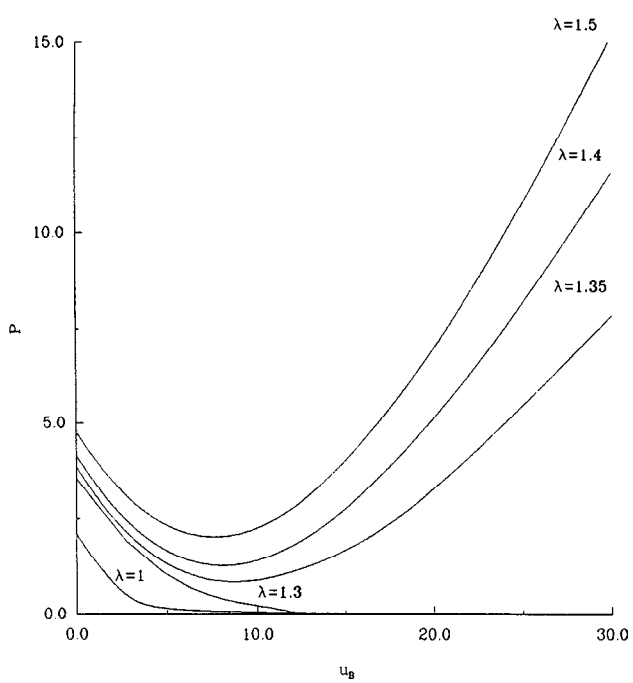

FIG. 11. P plotted versus Bondi time for various scales.

Figure 11 plots $P(\tilde{u})$ for several representative values of λ. The qualitative features of these graphs can be explained in terms of asymptotic results previously discussed. For the two graphs with $\lambda < \lambda_c$, P decays to zero as the system decays to flat space, in keeping with the role of P as a norm. For the three graphs with $\lambda > \lambda_c$, P exhibits interesting asymptotic behavior. First, at the initial time $\tilde{u} = 0$, these three graphs of P all have approximately the same slope. This is a manifestation of the high-amplitude relation (3.15) applied to the present case in which $Q = -Q_2 = \lambda$, so that $dP/d\tilde{u} \sim -\frac{2}{3}$ in the high-amplitude limit. For the value $\lambda = 2.5$, we find numerically that $dP/d\tilde{u}$ is initially -0.71. The high-amplitude limit (3.15) remains a good approximation to 10% accuracy even for values $\lambda \approx \lambda_c$. Also note that the presence of the Newman–Penrose constant Q_2 has a marked effect on the evolution, in this case driving P down at early times, even though the system ultimately forms a horizon. These three graphs each tend toward straight lines at large Bondi time, exhibiting the asymptotic relation (2.20), which implies that $dP/d\tilde{u} \to M_{\mathscr{H}}$. From the asymptotic slope of these graphs, it is evident that systems that start out at higher amplitude develop horizons with greater mass.

Figure 12 displays the evolution of the wave amplitude, in terms of plots of $g(u,x)$ at several values of the

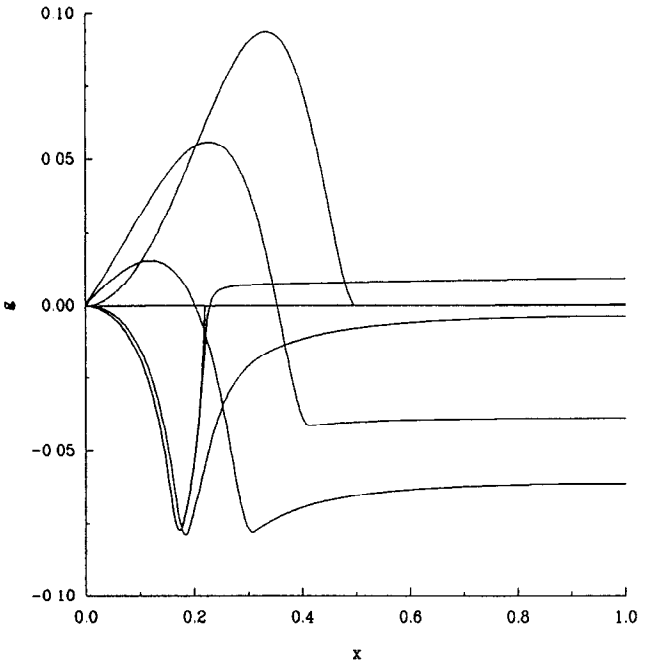

FIG. 13. Evolution of g for example B.

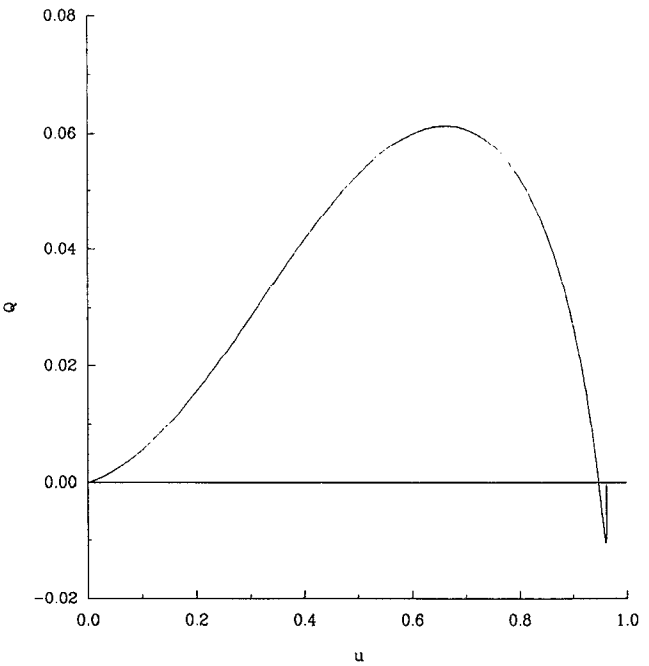

FIG. 14. Monopole decay for example B.

central time u, for $\lambda = 1.5$. Initially the waveform is the straight line $g(0,x) = x$. The time sequence is obvious from the formation of the cusp at $r = 2M_{\mathscr{H}}$. In the last profile, the "hair" outside $r = 2M_{\mathscr{H}}$ has been shed, except for a small neighborhood of J^+. Notice how this occurs while g maintains a constant slope at J^+, in accord with the conservation of Q_2. This illustrates the manner in which the conservation of the Newman–Penrose constant is consistent with the no-hair scenario. This same feature is also evident in the earlier example portrayed in Fig. 5, in which g has a constant negative slope at J^+, corresponding to a positive value of Q_2.

The decay of the monopole moment begins as in Fig. 7 with a long dive from its initial positive value followed by an upward bob beginning at some small negative value. However, in this case, Q bobs up to a positive value and then decays very sharply toward zero. Considerable numerical noise arises at these late times from the singularity developing at I^+, which leads to discretization error from the sharpness of the cusp and from roundoff error due to the high redshift. The code becomes unreliable when the redshift between central time and Bondi time is 10^9. In this example the large slope at J^+, corresponding to the large Newman–Penrose constant, contributes to the noise.

In order to translate dependence on central time into Bondi time it is necessary to know the time behavior of H. Although no rigorous derivation is known, a heuristic argument that seems to give the correct asymptotic time behavior of H can be based upon the qualitative features of the late stages of black hole formation that are evident in Fig. 12. Just before the formation of the horizon, the time and radial changes are dominated by the neighborhood of $r = 2M_{\mathscr{H}}$. This suggests the asymptotic approximation $g_{,r\tilde{u}} \sim 2M_{\mathscr{H}}\Phi_{,r\tilde{u}}$ whereby (2.17) leads to

$$\frac{dP}{d\tilde{u}} \sim 16\pi M_{\mathscr{H}}^2 \frac{d}{d\tilde{u}} \int_0^\infty r(\Phi_{,r})^2\, dr = 8M_{\mathscr{H}}^2 \frac{dH}{d\tilde{u}}, \quad (6.2)$$

where the last equality follows from the global integral of (2.5). Comparison with (2.20) then gives

$$H \sim \tilde{u}/8M_{\mathscr{H}}, \quad (6.3)$$

so that (2.4) implies

$$(u_H - u)/4M_{\mathscr{H}} \sim \exp(-\tilde{u}/4M_{\mathscr{H}}). \quad (6.4)$$

This is exactly analogous to the relation between Kruskal and Schwarzschild times. The relationship (6.3) is confirmed numerically to very convincing accuracy. A $(u_{\mathscr{H}} - u)^{1/2}$ monopole falloff then takes the form of an exponential decay with respect to Bondi time,

$$Q(\tilde{u}) \sim \text{const} \exp(-\tilde{u}/8M_{\mathscr{H}}). \quad (6.5)$$

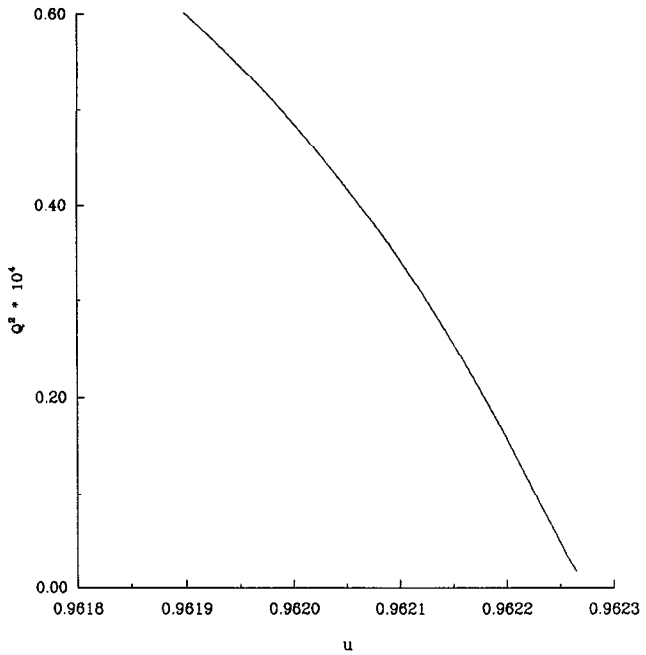

FIG. 15. The square of the monopole for example B.

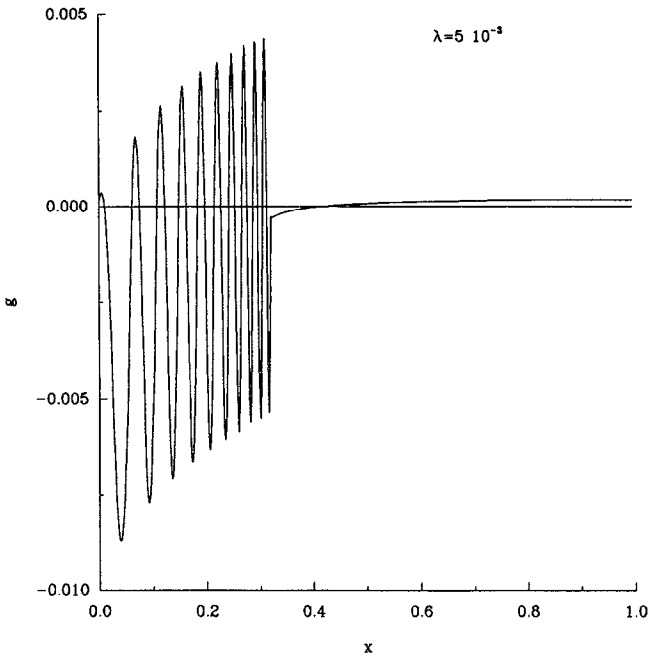

FIG. 17. Strong amplitude profile.

B. Example B

The one-parameter set of initial data,

$$\Phi(u_0,r)=\begin{cases}\lambda r(1-r)^2, & \text{for } r\leqslant 1,\\ 0, & \text{for } r\geqslant 1,\end{cases} \tag{6.6}$$

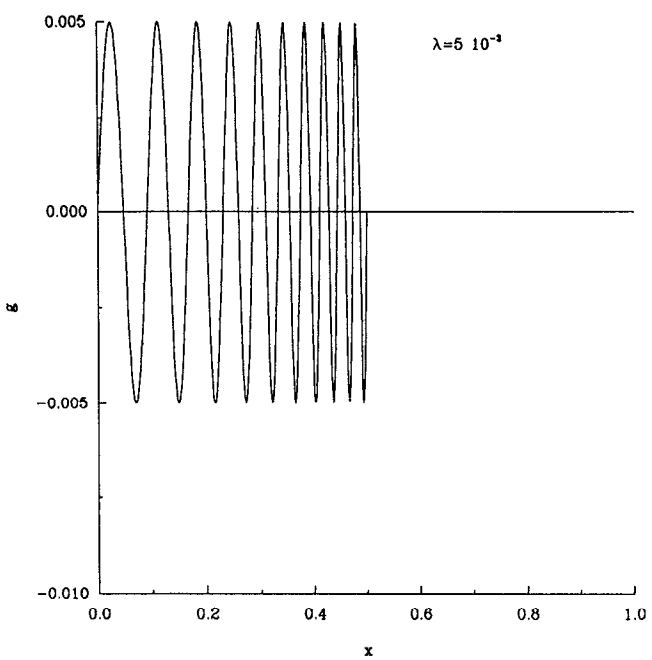

FIG. 16. The initial data for example B.

describes a pulse-shaped wave profile of compact support with critical value $\lambda_c \approx 1.3$. Figure 13 displays the evolution of $g(u,x)$ at several central times, for $\lambda = 1.5$. As the system collapse to a black hole, the formation of the cusp at $r = 2M_{\mathscr{H}}$, and the no-hair scenario is similar to the preceding examples. In this example, the conserved quantity $Q_2 = 0$ so that the slope of g vanishes at J^+. At the last time depicted in the figure, the field has completely vanished, to graphical accuracy, outside $r = 2M_{\mathscr{H}}$.

Figure 14 graphs the monopole moment versus central time. Initially the monopole vanishes but rises to some positive value. Then, as in the previous examples, there is a long dive to a small negative value followed by an upward bob. During this bob, the monopole moment decays toward zero without further oscillation. Figure 15 graphs $Q^2(u)$ during this final decay up to the time when the redshift reaches 10^5 and numerical noise is still negligible. During this interval, the graph of Q^2 approaches a straight line of finite slope, very accurately corroborating the $(u_{\mathscr{H}} - u)^{1/2}$ dependence hypothesized in Sec. V. The high accuracy here is possible due to the vanishing of the Newman–Penrose constant. Also, the asymptotic behavior of H, hypothesized in (6.3) is approached to within 2%, thus confirming the exponential relation (6.4) between central time and Bondi time. Approximately one-third of the initial mass is radiated in forming the black hole. Half this mass loss occurs during the initial period when the monopole moment is positive and the other half during the final bob.

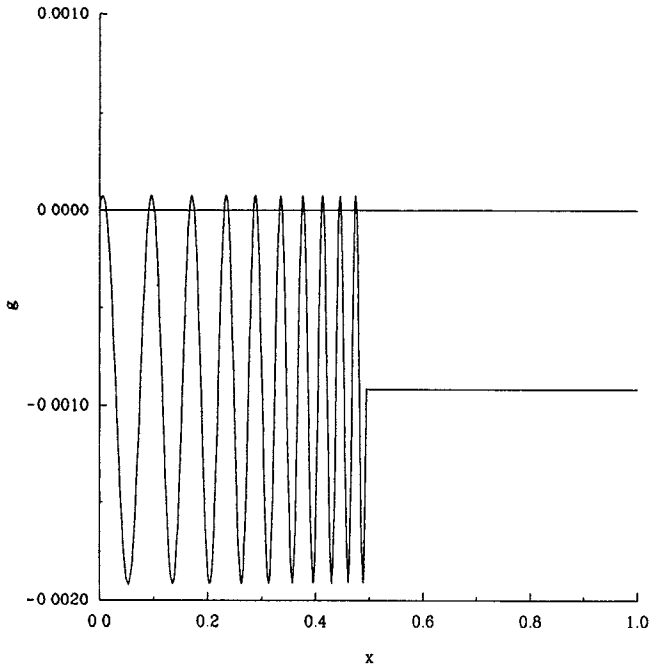

FIG. 18. Weak amplitude profile.

C. Example C

As a last example, consider the initial data,

$$\Phi(u_0,r)=\begin{cases}(\lambda/r)\sin(20\pi r), & \text{for } r\leqslant 1,\\ 0, & \text{for } r\geqslant 1.\end{cases} \tag{6.7}$$

Thus $g(u_0,r)$ consists of ten oscillations of equal amplitude, which are uniformly spaced with respect to r. The critical parameter value is $\lambda_c \approx 0.0019$.

Figure 16 graphs the initial profile of g vs x; Fig. 17 graphs g just before horizon formation in a strong amplitude case; and Fig. 18 graphs g in a weak amplitude case at a suitable time for comparison with the strong amplitude graph. The qualitative difference between Figs. 17 and 18 highlights the nonlinear effects of self-gravitation. The most striking feature of the strong amplitude case is that the horizon forms quite insensitively to the detailed structure of the field in the inner region $r < 2M_{\mathscr{H}}$. The chief difference, between the strong and weak case, in the evolution of g inside this inner region arises from the way in which the outgoing wave from the origin interferes with the incoming signal. In the weak case this interference lowers the entire profile in Fig. 18 by a constant determined by the amplitude of the outgoing wave leaving the origin at that time. In the strong case, backscattering couples the incoming and outgoing waves. The linear slope modulating the wave profile in Fig. 17 is a prime illustration of backscattering depleting the outgoing wave.

ACKNOWLEDGMENTS

It is a pleasure to thank Richard A. Isaacson for discussions. This work was supported by National Science Foundation Grant No. PHY-8803073. Computer time was provided by the Pittsburgh Supercomputing Center under Grant No. PHY860023P.

[1] R. H. Price, Phys. Rev. D **5**, 2419 (1972).
[2] E. T. Newman and R. Penrose, Proc. R. Soc. London Ser. A **305**, 175 (1968).
[3] C. W. Misner, K. S. Thorne, and J. A. Wheeler, *Gravitation* (Freeman, San Francisco, CA, 1973), p. 871.
[4] J. M. Bardeen and W. H. Press, J. Math. Phys. **14**, 7 (1972).
[5] D. Christodoulou, Commun. Math. Phys. **105**, 337 (1986).
[6] D. Christodoulou, Commun. Math. Phys. **106**, 587 (1986).
[7] D. Christodoulou, Commun. Math. Phys. **109**, 591 (1987).
[8] D. Christodoulou, Commun. Math. Phys. **109**, 613 (1987).
[9] R. A. Isaacson, J. S. Welling, and J. Winicour, J. Math. Phys. **24**, 1824 (1983).
[10] J. Winicour, in *Proceedings of the 3rd Canadian Conference on General Relativity and Relative Astrophysics*, edited by A. Coley, F. Cooperstock, and B. Tupper (World Scientific, Singapore, 1990), p. 94.
[11] C. M. Bender and S. A. Orszag, *Advanced Mathematical Methods for Scientists and Engineers* (McGraw-Hill, New York, 1978).
[12] D. S. Goldwirth and T. Piran, Phys. Rev. D **36**, 3575 (1987).
[13] M. W. Choptuik, in *Frontiers in Numerical Relativity*, edited by C. R. Evans, L. S. Finn, and D. W. Hobill, (Cambridge U.P., Cambridge, 1989).
[14] R. Gómez, R. A. Isaacson, J. S. Welling, and J. Winicour, in *Dynamical Space-Times and Numerical Relativity*, edited by Joan M. Centrella (Cambridge U.P., Cambridge, 1986), p. 236.
[15] R. Gómez, R. A. Isaacson, and J. Winicour, J. Comput. Phys. **98** (1992).
[16] A. Janis, E. T. Newman, and J. Winicour, Phys. Rev. Lett. **20**, 878 (1968).